



A theoretical study of 2D AlN on 3D C₄H₆N₆Ni₂ clathrate thermoelectric material composites

Ephraim M. Kiarii¹ · Krishna K. Govender^{1,2} · Penny P. Govender¹Received: 28 July 2019 / Accepted: 14 November 2019 / Published online: 19 November 2019
© Springer Nature Switzerland AG 2019

Abstract

Clean and green renewable energy is of paramount importance in the world today. Ab initio calculations using density functional theory demonstrate that superlattice structures can result into lowering lattice thermal conductivity and have improved electronic properties, which result in higher electrical conductivity. It is possible to achieve improved thermoelectricity-generating properties of materials with new superlattices and have large effective mass, as well as density of states at the Fermi level composed of 2D/2D AlN/C₄H₆N₆Ni₂. However, higher electrical conductivity requires high-mobility charge carriers, narrow-gap semiconductors and lower electron scattering. Thus, band structure, projected density of state, density of state, as well as spin density of state difference between alpha and beta eigenstates contributions, are used to reveal that heterostructures have advantage over the isolated materials. New superlattice structures would result in improving the charge generation/separation and yield a better thermoelectric material.

Keywords AlN · Clathrate · Heterostructures · First-principles calculations · Thermoelectricity

1 Introduction

Aluminium nitride (AlN) along with indium nitride and gallium nitride is a well-known wide energy gap semiconductor. However, due to the high energy of the surface optical phonons, AlN has become a prominent substrate for atomic layered composites [1]. The material is known to reduce remote interfacial phonon scattering, thereby improving the devices performance [1] to provide high charge mobility and dielectric constant [2]. The high thermal conductivity of AlN enables effective heat dissipation, which limit self-heating [3–5]. Its films can be reliably integrated [6] in large scale, for example 6" and 8" Si wafers [7, 8], making it both commercially and technologically significant for layered material production. In addition, de Almeida et al. [9] investigated the likelihood of apprehending two-dimensional (2D) hexagonal AlN by first-principles

density functional theory (DFT) calculations [9]. Furthermore, de Almeida et al.'s [9] first-principles calculations revealed stability of hexagonal-shaped AlN sheet. The simulations model system consisted of 96 atoms per supercell of a hexagonal AlN. De Almeida et al. predicted that AlN has an indirect gap of 2.81 eV and a cohesive energy, which is 6% lower than the bulk AlN.

Nickel diamminebis[m-(cyano-C:N)]bis(cyano-C) di (C₄H₆N₆Ni₂) clathrate is as a depiction of phonon glass–electron crystal materials; the clathrate structures have been studied for possible applications in thermoelectricity generation [10–15]. Type-I clathrate crystal structure is covalently bonded with the lattice composed of elements primarily from groups 13 and 14 of the periodic table. Its structure has cages, where metal atoms can fill in [13, 16]. Clathrate compounds have been found with high figure of merit (ZT) values of 1.35

✉ Penny P. Govender, pennyg@uj.ac.za | ¹Department of Chemical Sciences (Formally Applied Chemistry), University of Johannesburg, Doornfontein Campus, P.O. Box 17011, Johannesburg 2028, South Africa. ²Council for Scientific and Industrial Research, Meraka Institute, Centre for High Performance Computing, 15 Lower Hope Road, Rosebank, Cape Town 7700, South Africa.



at 900 K but contain expensive elements such as Ge and Ga in $\text{Ba}_8\text{Ga}_{16}\text{Ge}_{30}$ [17] crystal. About 46-mm-long crystal of the $\text{Ba}_8\text{Ga}_{16}\text{Ge}_{30}$ clathrate has been grown using Czochralski method [17, 18]. Saramat et al. [17] revealed electrical, thermal conductivities, as well as Seebeck coefficient transiting from extrinsic to intrinsic behaviour in the 600–900 K temperature range with ZT equal to 1.63 at 1100 K. Thus, $\text{Ba}_8\text{Ga}_{16}\text{Ge}_{30}$ clathrate is a strong candidate for high temperatures, as well as medium thermoelectric application. Efforts have also been made to include cheap elements such as Si and Al for thermoelectric application [19]. Bobnar et al. [19] developed and structurally studied $\text{Ba}_8\text{Al}_x\text{Si}_{46-x}$ clathrate-I phase, which revealed aluminium and silicon atoms: 5.7 aluminium atoms and 0.3 silicon atoms occupying the crystallographic site 6c, while 1.2 aluminium atoms and 22.8 Si atoms occupy site 24k. Further, atomic distribution was established using wavelength-dispersive X-ray spectroscopy [19], X-ray single-crystal diffraction [20], as well as NMR [19, 21] experiments. Condrón et al. [22] generated $\text{Ba}_8\text{Al}_{14}\text{Si}_{31}$ crystal using an aluminium flux method. Electron microprobe, ^{27}Al MAS NMR and single-crystal neutron diffraction were used to determine the aluminium site occupancies. However, Si-based clathrates show low ZT values. A cross-substitution improves the properties by introducing more scattering centres and changing the electronic band structure, thus bringing value to the basic investigative process of chemical composition, such as structural variations and stability [23–28].

Defects play a significant role in influencing the physical properties, as well as the applicability of materials [29–31]. Clathrate type-I structure has been observed for compounds containing defects, such as $\text{Rb}_8\text{Sn}_{442}$ and $\text{Ba}_8\text{Ge}_{433}$ [32, 33]. In these compounds, the defects can order in the crystal structure and give a superstructure belonging to $Ia\bar{3}d$ space group. At elevated temperatures, the defects randomise and a structural phase transition into the $Pm\bar{3}n$ structure is observed. From the experimental optical spectra study, schematic energy band for SrTiO_3 performed by Mishra et al. [34] revealed that the detection of oxygen defect is important from a technological point of view, as these vacancies are known to improve the photo-catalytic activities and magneto-optical properties. The idea of disorder and tunnelling states in the Sr and Eu systems but not in the Ba systems, and the corroborative nature of the difference Fourier nuclear density and lattice thermal conductivity has been established in the literature [35–37]. Chakoumakos et al. [38] revealed that Sr (2) in the large cage should have displacement parameters of one order of magnitude larger than that of the framework atoms and Sr (1) atom in the small cage. This addressed the guest atom disorder and dynamics in multi-temperature single-crystal and powder neutron diffraction study of

$\text{Sr}_8\text{Ga}_{16}\text{Ge}_{30}$. Difference Fourier maps with the Sr (2) atom removed from the reference model showed non-ellipsoidal features in the nuclear density with low density at the centre of the cage. These features in the nuclear density suggest a four-site disorder model. Refinements of single-crystal and the neutron powder diffraction data resulted in similar residual factors for models with four-site disorder on 24k or 24j, and this suggests that the disorder could be more complex than just four sites [39]. The metal atoms in cages, however, introduce low lattice thermal conductivity in clathrates [40–42]; the doped material results in high thermoelectric performance [43–45] as determined by $ZT = S^2\sigma T / (k_e + k_{ph})$. Where S , T and σ represent thermal power or Seebeck coefficient, the absolute temperature and electrical conductivity. Nevertheless, because of the inversion relationships between these parameters [46], it is challenging to improve thermoelectric performance by decreasing k or increasing S and σ . In this study, we investigate the traditional Clathrate $\text{C}_4\text{H}_6\text{N}_6\text{Ni}_2$ thermoelectric material with 2D AlN to form $\text{AlN}/\text{C}_4\text{H}_6\text{N}_6\text{Ni}_2$ heterostructures. Using ab initio methods, we study the geometry, electronic properties and optical properties to demonstrate that heterostructures can result in lowering lattice thermal conductivity, and can have improved electronic properties and reduced energy gap of composites, thus resulting in electrical conductivity increase. The study reveals the importance of heterostructures in electronic analysis, and demonstrates that improved electronic properties would lead to improving the charge generation and result in a better thermoelectric material.

2 Computational details

The ab initio calculations were made using the Cambridge Sequential Total Energy Package [47] program and employing Ultrasoft pseudopotentials as implemented in Biovia Materials Studio 2019 [48]. In this study, geometry optimisation, energy, electronic structure optical properties and charge generation and separation are computed. Additional functionals have been used to correct the underestimation of density functional theory. These include the generalised gradient approximation functional [49] with Perdure–Burke–Ernzerhof [50] to account for electron correlation effects. Geometry optimisation was done on ultra-fine quality with energy convergence tolerance of 5.0×10^{-6} eV/atom. The electronic cut-off energy was set at 400 eV with medium SCF tolerance. Discrete Fourier-transform algorithm [51] grid density was set at $42 \times 48 \times 160$. The convergence window was set mixing at three electronic densities with charge mixing amplitude of 0.5 having a charge mixing cut-off. The Monkhorst–Pack k -points to define the accuracy of the Brillouin zone sampling

were set at $8 \times 8 \times 1$ for energy, and Monkhorst–park grid $16 \times 16 \times 1$ k-point defined density of state (DOS) giving the actual spacing of $(0.00704 \times 0.000704 \times 0.05604)$ $1/\text{\AA}$. Spin mixing amplitude was set at 2.0 having a cut-off of $1.51/\text{\AA}$. To prevent the heterostructure layers from collapsing on each other, a vacuum slab was set at 20\AA and this allowed geometric relaxation.

3 Results and discussion

3.1 Computed models geometry

Many physical properties of crystals are associated with their point groups. Some of these properties are piezoelectricity, pyroelectricity, external morphology, ferroelectricity, optical activity or shape of the crystal, indices of refraction, as well as etch figures. A point group is a group of symmetry operations that leave at least one point of an object or pattern unmoved. In 2D, the elements of

the point group include the identity and may include one or more mirrors and/or one or more n -fold rotations. The symmetry operations are represented by matrices. $C_4H_6N_6Ni_2$ is a point group 4 with an order of four and four symmetry operations ($1, 2, 4^+$ and 4^-). Figure 1a shows an example of an abstract motif of $n(C_4H_6N_6Ni_2)$ with 3D tetragonal lattice length parameters of 7.235\AA , 8.310\AA along $(a=b, c)$, with a $P4/M$ spacegroup. The primitive cells angle symmetry constraints of $\alpha = \beta = \gamma = 90^\circ$, respectively, with the symmetry point group 4 and a projection of clathrate. $(C_6D_6)_{2n}$, catena-(bis(hexadeuterobenzene)) tetrakis(m2-cyano)-tetrakis(ammonio)-di-nickel clathrate) are also members having the same symmetry. In this study, we generated models of AlN with lattice parameters of $a=0.311$, $b=0.9385$ and $c=0.498$ nm, with a $Fm3m$ space group. The primitive cells atomistic position was set at $90^\circ, 90^\circ, 120^\circ$ for the α, β and γ , respectively [37], and built unit cells, which were magnified into supercells (Fig. 1b). Surfaces for reaction were cut along (101) (Fig. 1c) for $C_4H_6N_6Ni_2$ and layered heterostructures (Fig. 1d–f).

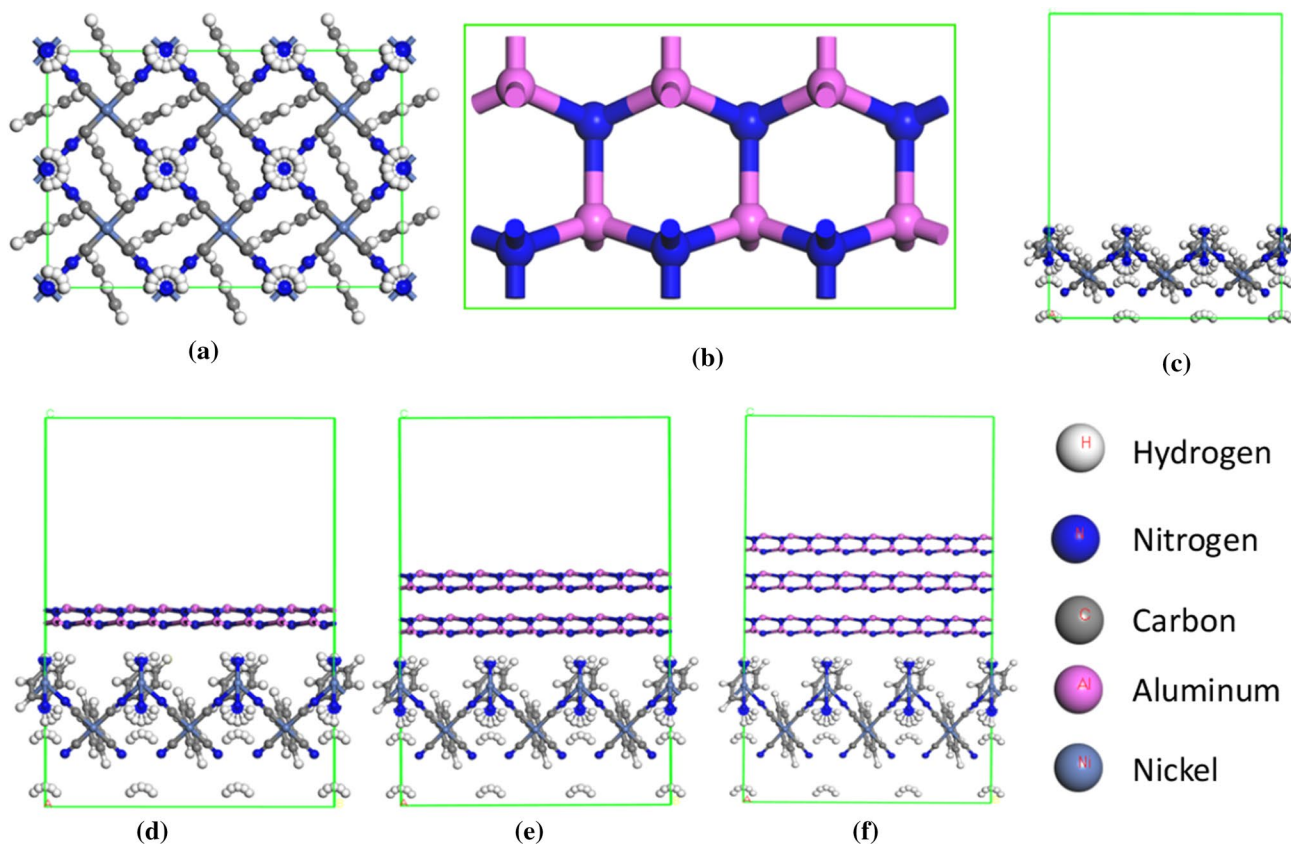


Fig. 1 Model structures of $C_4H_6N_6Ni_2$ (a), AlN (b), $C_4H_6N_6Ni_2$ surface (101) (c), $C_4H_6N_6Ni_2$ -AlN layer (d), $C_4H_6N_6Ni_2$ -AlN-AlN layer (e), $C_4H_6N_6Ni_2$ -AlN-AlN-AlN layer (f)

3.2 Electronic properties

3.2.1 Band structure

The electronic band energy structures were generated in order to find out the influence 2D AlN had on the formation of heterostructures. Since lowering heat conductivity requires scattering of acoustic phonons, this involves anisotropic thermal vibrations, inclusion of heavy atoms with complex structure, filling lattice cages with atoms for disorder, superlattice structures (heterostructures), as well as defects/grain boundary scattering. $C_4H_6N_6Ni_2$ had a zero band gap, and this can be ascribed to the high aromaticity of $C_4H_6N_6Ni_2$ structure, while AlN model had a direct band gap energy of 6.013 eV near the G point. This was much higher than the theoretically determined value by de Almeida et al. [9] (2.81 eV) and an experimental energy gap of 5.0 eV by Mattila et al. [52]. However, Li et al. [53] revealed a direct band gap of 6.12 eV near the G point of AlN from ab initio calculations. The experimental optical reflectance, as well as absorption/transmission cathode luminescence bandgap measurements, reported a 6.03 eV by Silveira et al. [54]. Furthermore, their study ascribes exciton at 6.03 eV and a shoulder intense line at 6.01 eV ascribed to the neutral donor-bound-exciton recombination. It was observed from our plot (Fig. 2) that the number of energy bands increased and induction of energy gap was observed in our heterostructures, i.e. $C_4H_6N_6Ni_2$ surface (2c), $C_4H_6N_6Ni_2$ -AlN layer

(0.015 eV) (2d), $C_4H_6N_6Ni_2$ -AlN-AlN layer (0.060) (2e) and $C_4H_6N_6Ni_2$ -AlN-AlN-AlN layer (0.022 eV) (2f). An energy gap is important in that the thermoelectric materials should not be a perfect conductor of heat. Temperature is dependent on band gap, and the optical band gap of semiconductors tends to decrease with the increase in temperature as found out by Mishra et al. [55]. However, the material requires being a good electrical conductor and the small energy gap created is enough to allow the electrons to move from valence band (VB) to conduction band (CB) with minimum energy.

3.2.2 Density of state (DOS)

Increasing Seebeck (α) can be archived by bandgap engineering, large DOS at $E=0$ and large effective mass. To understand the materials nature at the Fermi level, the DOS was calculated (Fig. 3a-e), i.e. $C_4H_6N_6Ni_2$, AlN, $C_4H_6N_6Ni_2$ -AlN layer, $C_4H_6N_6Ni_2$ -AlN-AlN layer and $C_4H_6N_6Ni_2$ -AlN-AlN-AlN layer. As shown in Fig. 3a, $C_4H_6N_6Ni_2$ material had increased degeneracy of band extrema. Furthermore, there was a clear lack of energy gap observed in $C_4H_6N_6Ni_2$. An intense decrease in the electron density of state at the Fermi level, i.e. zero energy AlN (Fig. 3b), was seen. The increase in extrema of heterostructures and high intensity in band structure can be ascribed to improve thermoelectric ZT as the Seebeck for the material is derived from the additions of contributions from each extremum [56, 57].

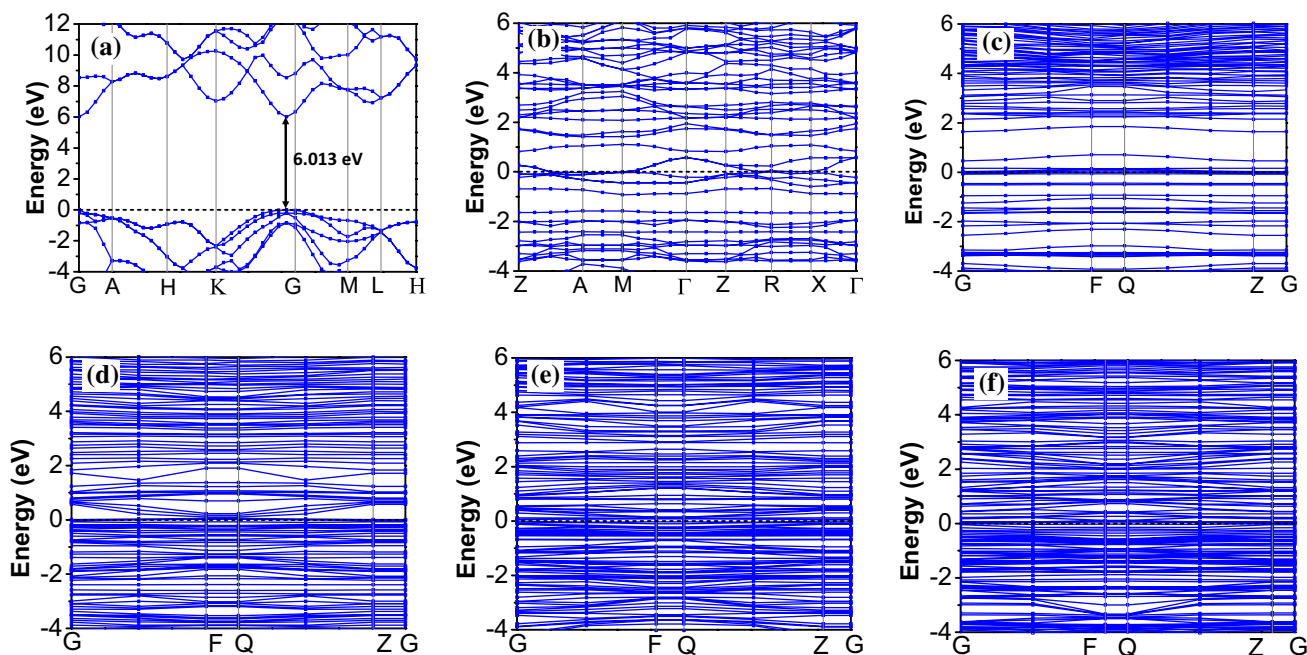


Fig. 2 Model structures of AlN (6.013 eV) (a), $C_4H_6N_6Ni_2$ (b), $C_4H_6N_6Ni_2$ surface (c), $C_4H_6N_6Ni_2$ -AlN layer (0.015 eV) (d), $C_4H_6N_6Ni_2$ -AlN-AlN layer (0.060) (e), $C_4H_6N_6Ni_2$ -AlN-AlN-AlN layer (0.022 eV) (f) represents the band structure, respectively

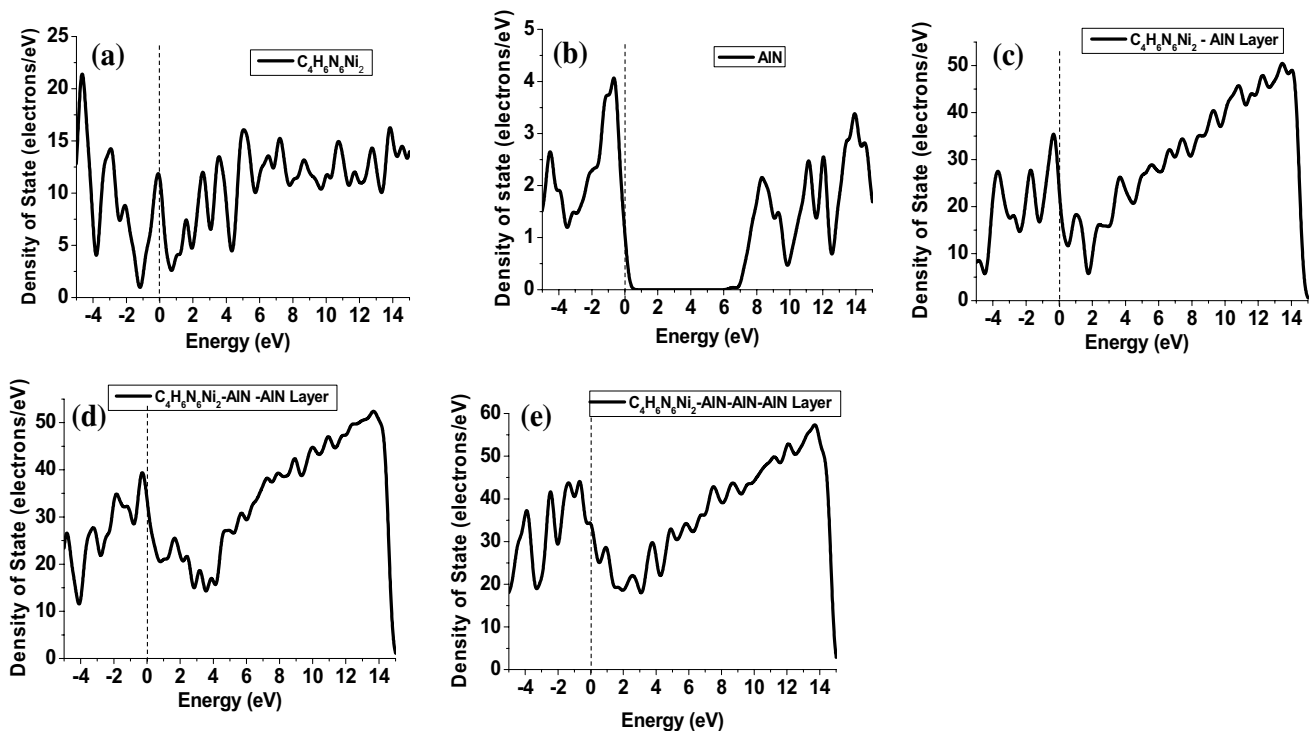


Fig. 3 Calculated $C_4H_6N_6Ni_2$ (a), AlN (b), $C_4H_6N_6Ni_2$ -AlN layer (c), $C_4H_6N_6Ni_2$ -AlN-AlN layer (d) and $C_4H_6N_6Ni_2$ -AlN-AlN-AlN layer (e) total densities of state ($E=0$ eV is set as the Fermi level (E_f), and this is represented by the perpendicular grey-dashed line)

3.2.3 Projected density of state (PDOS)

Individual element constituting our heterostructures was computed for their contribution to the interface projected as a plot of density of state (PDOS) (Fig. 4). Ni, C, N, H and Al projected density of state ($E=0$ eV is set as the Fermi level). Ni has an atomic number of 28 with $[Ar] 3d^8 4s^2$ or $[Ar] 3d^9 4s^1$ electronic configuration; it has 2, 8, 16, 2 or 2, 8, 17, 1 electron per shell. The $3d^8$ or $3d^9$ contribution was dominant in the VB, as well as conduction band past the Fermi level (Fig. 4a). However, the s orbital showed dominance past 3 eV into the conduction band. Carbon (C) has an electron configuration of $[He] 2s^2 2p^2$ (Fig. 4b) with 2, 4 electrons per shell, and its $2p^2$ in p orbital occupies the VB and CB with its highest electron density in the VB. N has an atomic number of 7 with $[He] 2s^2 2p^3$ electronic configuration, and it has 2, 5 electrons per shell.

The $2p^3$ contribution dominated in the VB, as well as in the conduction band past the Fermi level (Fig. 4c). However, it had the greatest contribution to the VB. Hydrogen has a symbol of H and atomic number 1. It has 1 electron per shell with electronic configuration of $1s^1$. It had an equal band contribution at the Fermi level. However, aluminium (Al) had the dominance in the conduction band with the $[Ne] 3s^2 3p^1$ electronic configuration, where the $3p^1$ orbital had the highest contribution at the Fermi level.

It was further observed that the p orbital contribution dominated the heterostructures generated from the individual elements $C_4H_6N_6Ni_2$, AlN, $C_4H_6N_6Ni_2$ -AlN, $C_4H_6N_6Ni_2$ -AlN-AlN and $C_4H_6N_6Ni_2$ -AlN-AlN-AlN layer partial density of state, respectively (Fig. 5), in both the valence and conduction bands. The influence of adding the different Al layers was observed by the increase in the DOS (electrons/eV), with Fig. 6e being the densest.

To explore the electron contribution and the orbitals near the Fermi level (E_f) at the interfaces of $C_4H_6N_6Ni_2$ -AlN, $C_4H_6N_6Ni_2$ -AlN-AlN and $C_4H_6N_6Ni_2$ -AlN-AlN-AlN heterostructures, the PDOS of bulk $C_4H_6N_6Ni_2$, AlN and their heterostructures were plotted (Fig. 5). The absence of bandgap in $C_4H_6N_6Ni_2$ is observed (Fig. 5a) with $4s^2$ or $4s^1$ electrons dominating both the VB and CB before and past E_f mainly from Ni (Fig. 5a). At the Fermi level, AlN VB is stuck at the $E=0$ eV of VB states with a clear separation (band gap) purely dominated by p orbital (Fig. 5b). N contributes $2p^3$ at VB, while the CB is made up of $3p^1$ from Al; this signifies upward band bending and p-type feature. The PDOS analysis of heterostructures from $C_4H_6N_6Ni_2$ and AlN shows that the VBM is largely contributed by $2p^3$, $4s^2$ or $4s^1$ states, respectively, while $3p^1$ makes the greatest contribution in CB. The electron transition from the VB to CB, i.e. $C_4H_6N_6Ni_2$ states to AlN states of in the composite reveal the orbitals involved and their influence in thermal

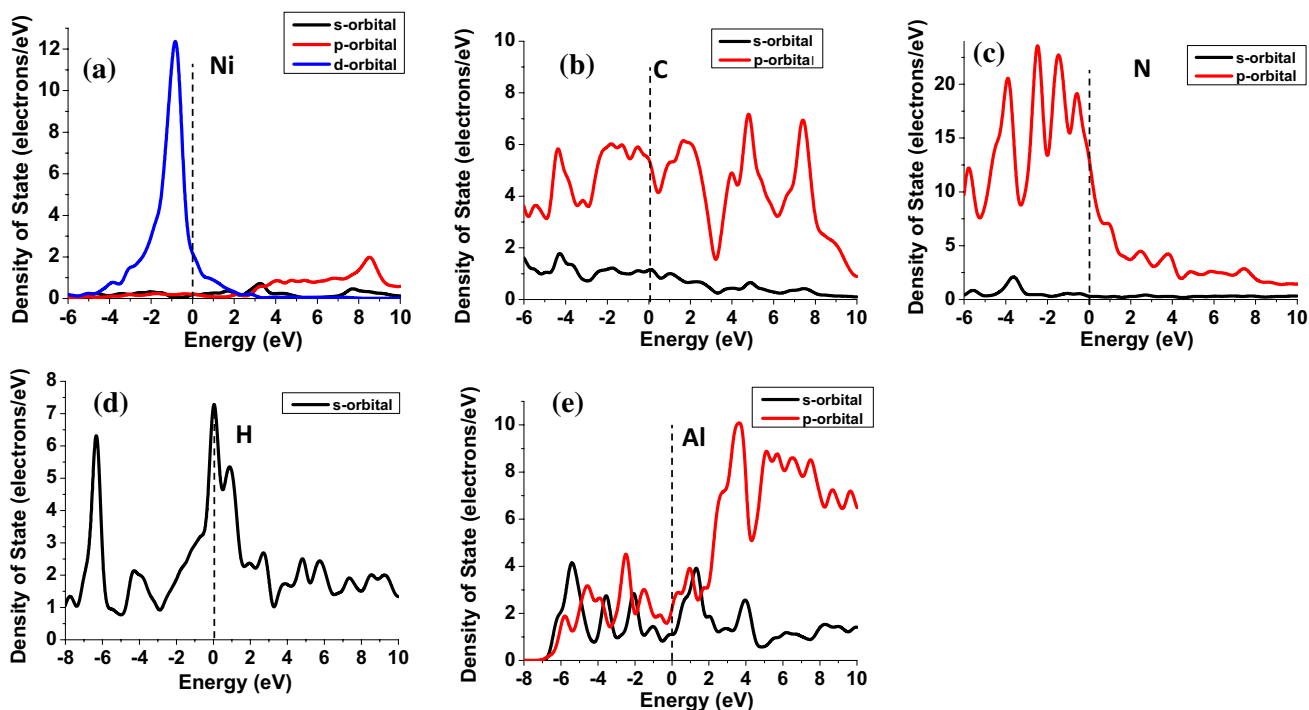


Fig. 4 Calculated individual element Ni, C, N, H and Al projected density of state ($E=0$ eV is set as the Fermi level (E_f), and this is represented by perpendicular grey-dashed line)

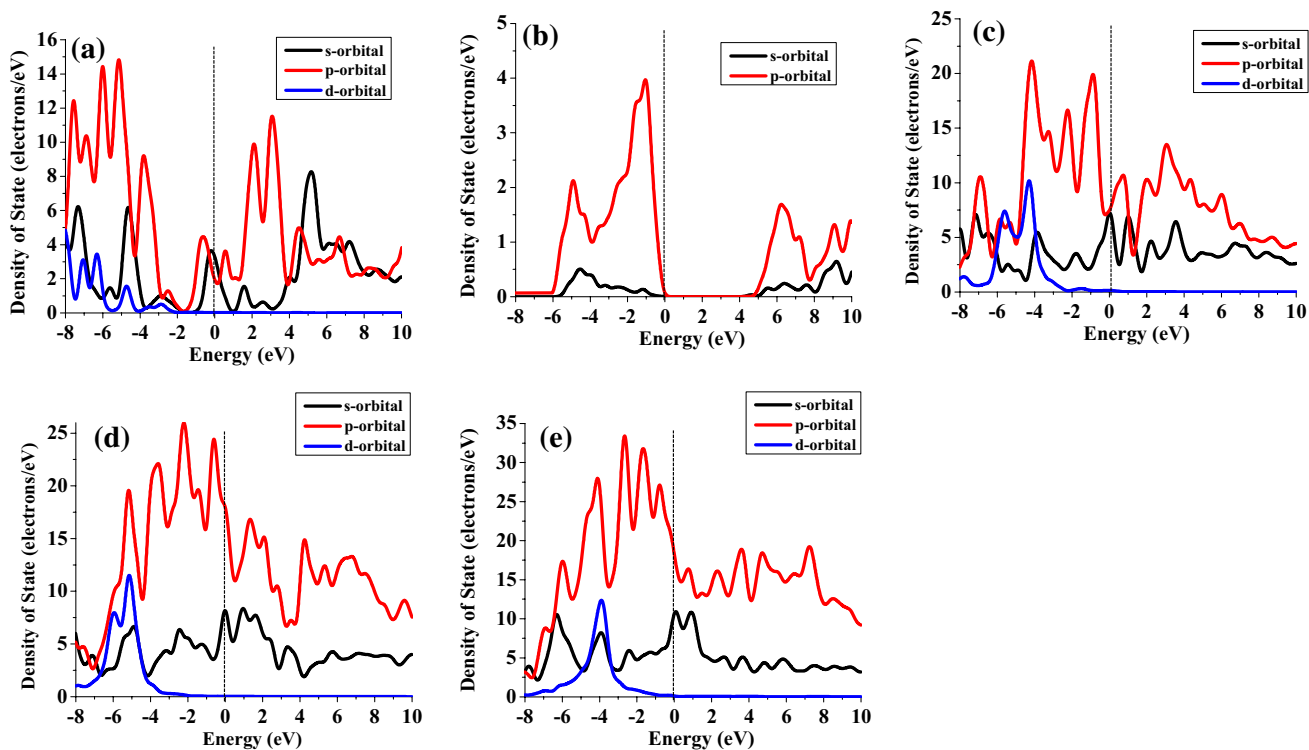


Fig. 5 Calculated $C_4H_6N_6Ni_2$ (a), AlN (b), $C_4H_6N_6Ni_2$ -AlN layer (c), $C_4H_6N_6Ni_2$ -AlN-AlN layer (d) and $C_4H_6N_6Ni_2$ -AlN-AlN-AlN layer (e). Partial density of state, respectively ($E=0$ eV is set as the Fermi level (E_f), and this is represented by perpendicular grey-dashed line)

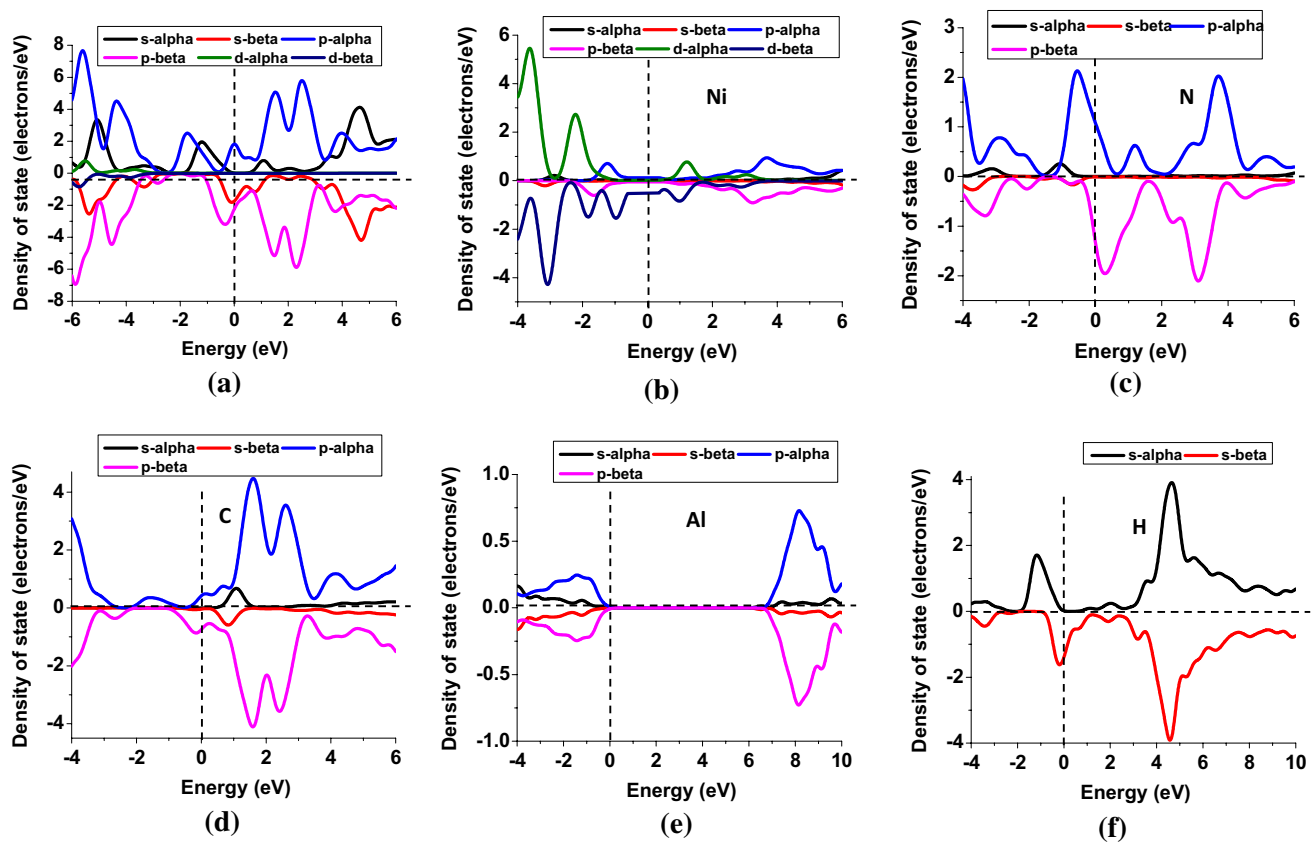


Fig. 6 Calculated $C_4H_6N_6Ni_2$ -AlN layer (a) and individual element Ni, N, C, Al, and H spin density of state, respectively ($E=0$ eV is set as the Fermi level (E_f), and this is represented by perpendicular grey-dashed line)

electron generation or light absorption [15]. Therefore, from Fig. 5c–e, the VB of composites is dominated by p orbital states, as well as the CBM in layer. There is a distinct increase in the density of state of the layer build up, resulting in an increase with both VB and CB, respectively. Under heat (infrared) or visible light, it is possible for the electrons in the $C_4H_6N_6Ni_2$ states to be easily transferred into the AlN states.

3.3 Spin density of state

The $C_4H_6N_6Ni_2$ -AlN monolayer and Ni, N, C, Al, and H spin density of state of starting materials were calculated and analysed using DFT against individual components and plotted in the state graph density. In the spin-polarised calculation, individual states contributions from alpha and beta were summarised. The spin-up contributions formed only self-states alpha, and only self-states spin-down made beta. The results and the difference in beta and alpha contributions were shown in a butterfly plot (Fig. 6). Ni, N, C, Al, and H had equal spin-down and spin-up energies. Despite the fact that all the elements had equal alpha and beta spins as observed (Fig. 6a), the composite shows

slight shift at the Fermi level and this can be ascribed to the doping effect as seen in the emergence of a bandgap in the composites in the band structures.

3.4 The optical properties

New material gives a wealth of information about the low-energy excitations that govern the physics of material. Some of these excitations indicate the part of the solar spectrum, where they might be expected to appear. A number of quantities, often called optical constants, describe the response of materials to light/heat. These optical constants, such as the dielectric constant (ϵ), the electrical conductivity (σ), the susceptibility (χ) and the refractive index (n) among others, are neither constant nor independent but are functions of the pressure, external magnetic field, frequency, as well as temperature. By knowing two of these, one that describes the absorption in the solid and one that describes dispersion, all of the others may be calculated using Maxwell's [58, 59] equations for macroscopic media as expressed using Gaussian units [60].

The value of reflectivity as a function of an incident angle is calculated using Fresnel’s formulas [61] from absorption index of sample material and refractive index. Our calculated reflectivity against wavelength plot reveals that at low wavelengths, i.e. below 200 nm (Fig. 7a), AlN is the highest. Single-layered heterostructure resulted in a drop in the reflectance, and subsequent addition of the layers show improvement in reflectivity with the C₄H₆N₆Ni₂-AlN-AlN-AlN layer having the highest reflectivity from 240 nm into the redshift.

Absorption is the process of converting radiant energy into internal energy of the medium. This occurs by two: mainly by Rayleigh scattering [62] and Compton scattering [63]. Thermoelectric effect occurs when photon/heat energy is consumed to release an electron from atom nucleus [64]. This effect arises from the fact that the potential energy barrier for electrons is finite at the surface of the material. AlN (Fig. 7b) has the least absorption, which mainly occurs in the ultraviolet region of the solar spectrum. Improvement was observed when the layered heterostructures were tested with the three

layers being the highest at all wavelengths tested, i.e. 200 to 2500 nm.

The calculated optical conductivity (Fig. 7c) showed C₄H₆N₆Ni₂ exhibits a high conductivity in the high-frequency region of the solar spectrum; thus, as the wavelength increases the conductivity decreased in a uniform manner. However, a significant improvement in the conductivity with increase in layers was noted particularly at higher wavelengths with C₄H₆N₆Ni₂-AlN-AlN-AlN layer dominating. Thermoelectric materials require high electrical conductivity. Increasing electrical conductivity (σ) entails having a material with high charge carrier mobility, narrow energy gap semiconductors. To lower electron scattering, our calculated electrical conductivity (Table 1) using the Boltzmann constant relation [65] is as follows:

$$\sigma = \sigma_0 \exp\left(-\frac{E_a}{k_T}\right)$$

where σ_0 is a constant, E_a is the activation energy and k is Boltzmann constant. This show a gradual decrease in conductivity from the thermoelectric material C₄H₆N₆Ni₂

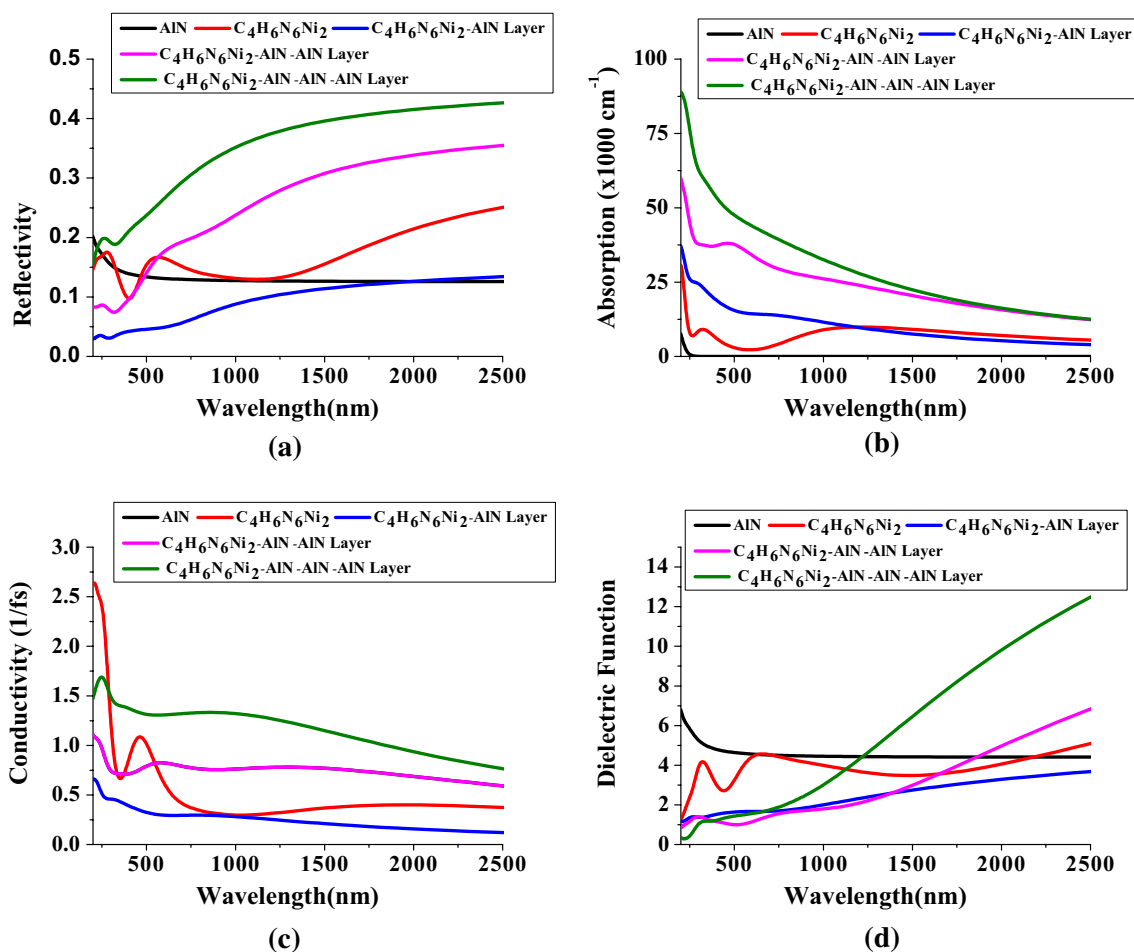


Fig. 7 Calculated optical properties of the C₄H₆N₆Ni₂ and AlN as well as the heterostructures

Table 1 Calculated electrical conductivity of AlN, $C_4H_6N_6Ni_2$ and the composites

Compound	Band gap	Electrical conductivity
AlN	6.010	3.300×10^{-51}
$C_4H_6N_6Ni_2$ surface (101)	0	1
$C_4H_6N_6Ni_2$ -AlN layer	0.015	0.748
$C_4H_6N_6Ni_2$ -AlN-AlN layer	0.060	0.313
$C_4H_6N_6Ni_2$ -AlN-AlN-AlN layer	0.022	0.653

surface (101) with single layer to double layers; however, the three-layer system indicated an increase in conductivity and this can be ascribed to a reduction in electron affinity and ionisation energy as observed.

Our study of the permittivity of a material as function of frequency (dielectric function) (Fig. 7d) is derived from Maxwell's equations, which state that a dielectric-metallic interface can support surface plasmon polaritons. Unique properties of interface waves arise and are the result of dielectric materials optical frequency-dependent dispersion characteristics. At higher wavelength above 1250 nm, $C_4H_6N_6Ni_2$ -AlN-AlN-AlN layer showed a high dielectric function. However, the absence of negative permittivity means that the electric displacement vector and the electric field vector point in the same direction. The high wavelengths are appropriate for thermoelectric application indicating improvement in the generated composites having probable infrared wavelength of red heat.

3.5 Mechanism of charge transfer

To understand the charge transfer mechanism between the layers within heterostructures generated, electron density difference is necessary [66]. This will explain the observation on what happens when two surfaces interact. The interfacial interactions are expected to change the charge distribution between surfaces, which result in charge transfer across the heterostructures.

In order to explore the charge transfer process in the $C_4H_6N_6Ni_2$ -AlN and $C_4H_6N_6Ni_2$ -AlN-AlN heterostructures, three-dimensional charge density difference (Fig. 8) is plotted with the yellow iso-surface representing electron accumulation, while the green iso-surface represents the electron depletion with an iso-surface value of 0.003 \AA^{-3} . Figure 8 reveals that the charge densities are redistributed by forming hole- and electron-rich regions within the bulk $C_4H_6N_6Ni_2$, $C_4H_6N_6Ni_2$ surface (101) and AlN sheet interface. This is attributed to the large separation between the AlN sheet and $C_4H_6N_6Ni_2$ surface (101). In addition, a high charge depletion occurred on the bulk $C_4H_6N_6Ni_2$ accumulating on $C_4H_6N_6Ni_2$ surface (101), resulting in hole-rich $C_4H_6N_6Ni_2$ sites. Thus, holes accumulated in the $C_4H_6N_6Ni_2$

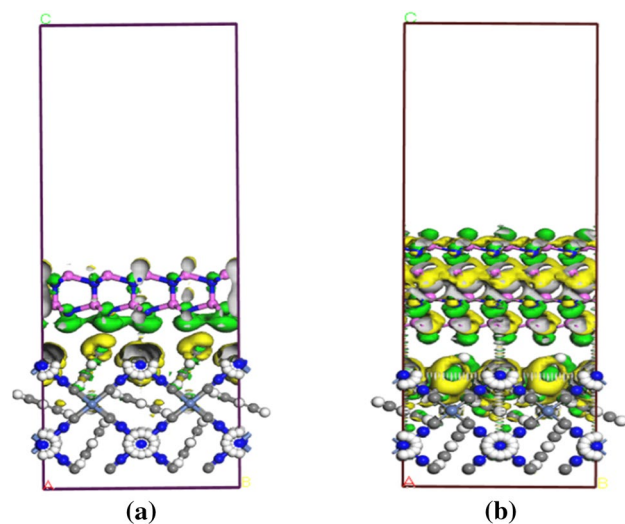


Fig. 8 Calculated charge density difference of $C_4H_6N_6Ni_2$ -AlN layer and $C_4H_6N_6Ni_2$ -AlN-AlN layer with an iso-surface of 0.003 \AA^{-3} (the yellow iso-surface represents electron accumulation, while the green iso-surface represents the electron depletion)

bulk region, while electrons accumulated in the region close to the surfaces; therefore, electrons are expected to be excited from the $C_4H_6N_6Ni_2$ to the surface (101) and crossover to AlN. $C_4H_6N_6Ni_2$ acts as electron donor and conduction medium to transport electrons to the AlN surface.

The $C_4H_6N_6Ni_2$ -AlN (Fig. 8a) and $C_4H_6N_6Ni_2$ -AlN-AlN layer (Fig. 8b) differences in electron density show the Mulliken population analysis [67, 68], and the three-dimensional charge density difference [66] confirms the transfer of interlayer charge between the $C_4H_6N_6Ni_2$ -AlN monolayers as previously observed in PDOS analysis. The charge density difference in the two-layer system (Fig. 8b) shows a strong charge relocation at the AlN interface region, which can lead to substantial quantities of charge generation in $C_4H_6N_6Ni_2$ and subsequent transfer increase in the layers, resulting in more charge accumulation in the AlN. This study, therefore, reveals that the interaction at the interface causes not only strong charge distribution fluctuation in each component, but also significant interfacial charge transfer and separation of heterostructures, which determine the mechanism of the enhanced thermos-catalytic performance of the heterostructures.

3.6 Electron affinity and ionisation energy

$C_4H_6N_6Ni_2$, AlN and their heterostructures were calculated for their electron-transporting properties (Fig. 9). The ionisation energy was obtained from work function + E_{VBM} [69], where $E_{VBM} = -\text{Work function} + 0.5 \text{ energy gap}$ [70] and Electron affinity = ionisation potential-band gap [71].

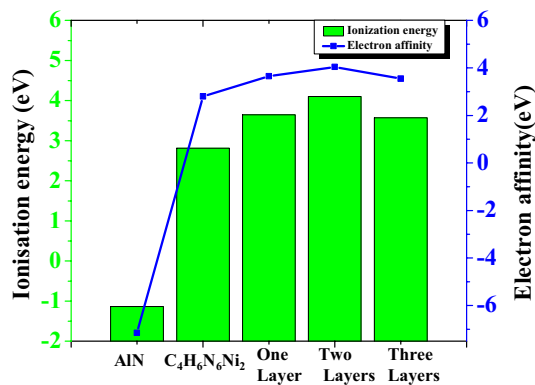


Fig. 9 Calculated ionisation energy and electron affinity of AlN, C₄H₆N₆Ni₂, C₄H₆N₆Ni₂-AlN layer (one layer), C₄H₆N₆Ni₂-AlN-AlN layer (two layers) and C₄H₆N₆Ni₂-AlN-AlN-AlN layer (three layers) along the x-axis

Energies of the band edges and vacuum level were used in calculations of electron affinity and ionisation energy of the individual monolayers as well as their corresponding heterostructures.

The calculated ionisation energy and electron affinity of AlN, C₄H₆N₆Ni₂, C₄H₆N₆Ni₂-AlN layer, C₄H₆N₆Ni₂-AlN-AlN layer and C₄H₆N₆Ni₂-AlN-AlN-AlN layer along the x-axis are shown in Fig. 9. AlN had the least ionisation energy of -1.135 eV, which was followed by C₄H₆N₆Ni₂ with 2.814 eV. Generating a single layer resulted in a further increase in the ionisation energy to a maximum value of 4.102 eV in the two layers. However, after generating two layers, the three layers of AlN resulted in a reduction in the ionisation energy, where a similar trend was observed with the least being -7.145 eV and the maximum electron affinity was 4.042 eV. The reduction in the three-layer system can be ascribed to the shielding effect and the distance from the thermoelectric material. Thus, it will be easy to move an electron from the thermoelectric material into AlN in the composite generated.

4 Conclusion

Using first-principles calculations, we demonstrate that it is possible to generate layered C₄H₆N₆Ni₂-AlN heterostructures with increased electrical conductivity and reduced thermal conductivity because of superlattice structures. The new heterostructures resulted in improved properties, such as large effective mass, new energy gaps and large density of states at the Fermi level. Increasing electrical conductivity requires high-mobility charge carriers, narrow-gap semiconductors and lower electron scattering. Optical and electronic properties revealed improvement in the electron density of state, conductivity and dielectric

function. The benefit arising from the improved electronic properties would lead to improving the charge generation and separation, thus resulting in a better thermoelectric material.

Acknowledgements The authors would like to acknowledge the financial contributions from the Faculty of Science: University of Johannesburg, South Africa: Centre for Nanomaterials Science Research, Department of chemical sciences and the National Research Foundation (TTK14052167682). EMK acknowledges the financial support from URC International Scholarship from the University of Johannesburg. The authors are also grateful to the Centre for High Performance Computing (CHPC) for computational resources provided.

Compliance with ethical standards

Conflict of interest The authors declare that they have no conflict of interests.

References

1. Gun OhJ, Ki Hong S, Kim C-K, Hoon Bong J, Shin J, Choi S-Y, Jin Cho B (2014) High performance graphene field effect transistors on an aluminum nitride substrate with high surface phonon energy. *Appl Phys Lett* 104(19):193112
2. Ma N, Jena D (2014) Charge scattering and mobility in atomically thin semiconductors. *Phys Rev X* 4(1):011043
3. Perebeinos V, Avouris P (2010) Inelastic scattering and current saturation in graphene. *Phys Rev B* 81(19):195442
4. Freitag M, Steiner M, Martin Y, Perebeinos V, Chen Z, Tsang JC, Avouris P (2009) Energy dissipation in graphene field-effect transistors. *Nano Lett* 9(5):1883–1888
5. Bae M, Islam S, Dorgan V, Pop E (2011) Scaling of high-field transport and localized heating in graphene transistors. *ACS Nano* 5(10):7936–7944
6. Chandrasekar H, Mohan N, Bardhan A, Bhat K, Bhat N, Ravishankar N, Raghavan S (2013) An early in situ stress signature of the AlN-Si pre-growth interface for successful integration of nitrides with (111) Si. *Appl Phys Lett* 103(21):211902
7. Li J, Lin J, Jiang H (2006) Growth of III-nitride photonic structures on large area silicon substrates. *Appl Phys Lett* 88(17):171909
8. Ng GI, Arulkumaran S, Vicknesh S, Wang H, Ang K, Kumar CM, Ranjan K, Lo G-Q, Tripathy S, Boon CC (2012) GaN-on-silicon integration technology. In: 2012 IEEE international symposium on radio-frequency integration technology (RFIT). IEEE, pp 159–161
9. de Almeida E, de Brito Mota F, de Castilho C, Kakanakova-Georgieva A, Gueorguiev GK (2012) Defects in hexagonal-AlN sheets by first-principles calculations. *Eur Phys J B* 85(1):1–9
10. Nolas G, Cohn J, Slack G, Schujman S (1998) Semiconducting Ge clathrates: promising candidates for thermoelectric applications. *Appl Phys Lett* 73(2):178–180
11. Ikeda M, Euchner H, Yan X, Tomeš P, Prokofiev A, Prochaska L, Lientschnig G, Svagera R, Hartmann S, Gati E (2019) Kondo-like phonon scattering in thermoelectric clathrates. *Nat Commun* 10(1):887
12. Kaur P, Madsen GK, Bera C (2019) Thermoelectric figure of merit and thermal conductivity of type-I clathrate alloy nanowires. *MRS Commun* 9(1):370–374
13. Dong Y, Ding X, Yan X, Zhang L, Ju T, Liu C, Rogl P, Paschen S (2019) Structural and thermoelectric properties of Cu substituted Type I clathrates Ba₈Cu_xSi_{32-x}Ga₁₄. *Materials* 12(2):237

14. Grin Y (2019) Inhomogeneity and anisotropy of chemical bonding and thermoelectric properties of materials. *J Solid State Chem* 274:329–336
15. Yang J, Wang Y, Yang H, Tang W, Yang J, Chen L, Zhang W (2019) Thermal transport in thermoelectric materials with chemical bond hierarchy. *J Phys: Condens Matter* 31(18):183002
16. Rogl P (2006) Formation and crystal chemistry of clathrates. In: Rowe DM (ed) *Thermoelectrics handbook: macro to nano*. CRC Press, Boca Raton
17. Saramat A, Svensson G, Palmqvist A, Stiewe C, Mueller E, Platzek D, Williams S, Rowe D, Bryan J, Stucky G (2006) Large thermoelectric figure of merit at high temperature in Czochralski-grown clathrate $\text{Ba}_8\text{Ga}_{16}\text{Ge}_{30}$. *J Appl Phys* 99(2):023708
18. Kitamura K, Yamamoto J, Iyi N, Kirnura S, Hayashi T (1992) Stoichiometric LiNbO_3 single crystal growth by double crucible Czochralski method using automatic powder supply system. *J Cryst Growth* 116(3–4):327–332
19. Bobnar M, Böhme B, Wedel M, Burkhardt U, Ormeci A, Prots Y, Drathen C, Liang Y, Nguyen HD, Baitinger M (2015) Distribution of Al atoms in the clathrate-I phase $\text{Ba}_8\text{Al}_x\text{Si}_{46-x}$ at $x = 6.9$. *Dalton Trans* 44(28):12680–12687
20. Christensen M, Lock N, Overgaard J, Iversen BB (2006) Crystal structures of thermoelectric n- and p-type $\text{Ba}_8\text{Ga}_{16}\text{Ge}_{30}$ studied by single crystal, multitemperature, neutron diffraction, conventional X-ray diffraction and resonant synchrotron X-ray diffraction. *J Am Chem Soc* 128(49):15657–15665
21. Webb GA (1979) C. P. Slichter. Principles of magnetic resonance. Springer series in Solid-State Sciences, Vol. 1, Ed by M. Cardoua, P. Fulde and H. J. Queisser, Springer-Verlag, Berlin (1978). 397 pages. DM 54, US\$7.00. *Organ Magn Reson* 12(3):IV. <https://doi.org/10.1002/mrc.1270120316>
22. Condrón CL, Martin J, Nolas G, Piccoli PM, Schultz AJ, Kauzlarich SM (2006) Structure and thermoelectric characterization of $\text{Ba}_8\text{Al}_{14}\text{Si}_{31}$. *Inorg Chem* 45(23):9381–9386
23. Yan X, Bauer E, Rogl P, Paschen S (2013) Structural and thermoelectric properties of $\text{Ba}_8\text{Cu}_5\text{Si}_x\text{Ge}_{41-x}$ clathrates. *Phys Rev B* 87(11):115206
24. Xu J, Wu J, Heguri S, Mu G, Tanabe Y, Tanigaki K (2012) Low-temperature physical properties of $\text{Ba}_8\text{Ni}_x\text{Ge}_{46-x}$ ($x = 3, 4, 6$). *J Electron Mater* 41(6):1177–1180
25. Shi X, Yang J, Bai S, Yang J, Wang H, Chi M, Salvador JR, Zhang W, Chen L, Wong-Ng W (2010) On the design of high-efficiency thermoelectric clathrates through a systematic cross-substitution of framework elements. *Adv Funct Mater* 20(5):755–763
26. Falmbigl M, Grytsiv A, Rogl P, Heinrich P, Royanian E, Bauer E (2013) Tuning of band gap and thermoelectric properties of type-I clathrate $\text{Ba}_8\text{Ni}_x\text{Zn}_y\text{Ge}_{46-x-y-z}\text{Sn}_z$. *J Alloys Compd* 567:65–72
27. Sirusi AA, Ross JH, Yan X, Paschen S (2015) NMR study of $\text{Ba}_8\text{Cu}_5\text{Si}_x\text{Ge}_{41-x}$ clathrate semiconductors. *Phys Chem Chem Phys* 17(26):16991–16996
28. Ångqvist M, Lindroth DO, Erhart P (2016) Optimization of the thermoelectric power factor: coupling between chemical order and transport properties. *Chem Mater* 28(19):6877–6885
29. Jupille J, Thornton G (2015) Defects at oxide surfaces. In: Jacques J, Geoff T (eds) *Springer series in surface sciences*, vol 58. Springer, Cham
30. von Oertzen GU, Gerson AR (2007) The effects of O deficiency on the electronic structure of rutile TiO_2 . *J Phys Chem Solids* 68(3):324–330
31. Mishra V, Warshi MK, Sati A, Kumar A, Mishra V, Sagdeo A, Kumar R, Sagdeo PR (2018) Diffuse reflectance spectroscopy: an effective tool to probe the defect states in wide band gap semiconducting materials. *Mater Sci Semicond Process* 86:151–156
32. Carrillo-Cabrera W, Budnyk S, Prots Y, Grin Y (2004) $\text{Ba}_8\text{Ge}_{43}$ revisited: a $2a' \times 2a' \times 2a'$ superstructure of the Clathrate-I type with full vacancy ordering. *Z Anorg Allg Chem* 630(13–14):2267–2276
33. Kaltzoglou A, Fässler T, Christensen M, Johnsen S, Iversen B, Presniakov I, Sobolev A, Shevelkov A (2008) Effects of the order-disorder phase transition on the physical properties of $\text{A}_8\text{Sn}_{44}\square_2$ ($A = \text{Rb}, \text{Cs}$). *J Mater Chem* 18(46):5630–5637
34. Mishra V, Sati A, Warshi MK, Phatangare AB, Dhole S, Bhoraskar V, Ghosh H, Sagdeo A, Mishra V, Kumar R (2018) Effect of electron irradiation on the optical properties of SrTiO_3 : an experimental and theoretical investigations. *Mater Res Express* 5(3):036210
35. Zerec I, Keppens V, McGuire M, Mandrus D, Sales BC, Thalmeier P (2004) Four-well tunneling states and elastic response of clathrates. *Phys Rev Lett* 92(18):185502
36. Suekuni K, Avila M, Umeo K, Takabatake T (2007) Cage-size control of guest vibration and thermal conductivity in $\text{Sr}_8\text{Ga}_{16}\text{Si}_{30-x}\text{Ge}_x$. *Phys Rev B* 75(19):195210
37. Avila M, Suekuni K, Umeo K, Fukuoka H, Yamanaka S, Takabatake T (2006) Glasslike versus crystalline thermal conductivity in carrier-tuned $\text{Ba}_8\text{Ga}_{16}\text{X}_{30}$ clathrates ($X = \text{Ge}, \text{Sn}$). *Phys Rev B* 74(12):125109
38. Chakoumakos B, Sales B, Mandrus D, Nolas G (2000) Structural disorder and thermal conductivity of the semiconducting clathrate $\text{Sr}_8\text{Ga}_{16}\text{Ge}_{30}$. *J Alloys Compd* 296(1–2):80–86
39. Christensen M, Johnsen S, Iversen BB (2010) Thermoelectric clathrates of type I. *Dalton Trans* 39(4):978–992
40. Nolas G, Weakley T, Cohn J, Sharma R (2000) Structural properties and thermal conductivity of crystalline Ge clathrates. *Phys Rev B* 61(6):3845–3850
41. Nolas GS, Chakoumakos BC, Mahieu B, Long GJ, Weakley T (2000) Structural characterization and thermal conductivity of type-I tin clathrates. *Chem Mater* 12(7):1947–1953
42. Fässler TF (2011) Zintl phases: principles and recent developments, vol 139. Springer, Heidelberg
43. DiSalvo FJ (1999) Thermoelectric cooling and power generation. *Science* 285(5428):703–706
44. Cole T (1983) Thermoelectric energy conversion with solid electrolytes. *Science* 221(4614):915–920
45. Wood C (1988) Materials for the thermoelectric energy conversion. *Rep Prog Phys* 51(4):459
46. Snyder GJ, Toberer ES (2011) Complex thermoelectric materials. In: Dusastre V (ed) *Materials for sustainable energy: a collection of peer-reviewed research and review articles from Nature Publishing Group*. World Scientific, Singapore, pp 101–110
47. Segall MD, Philip JDL, Probert MJ, Pickard CJ, Hasnip PJ, Clark SJ, Payne MC (2002) First-principles simulation: ideas, illustrations and the Castep code. *J Phys: Condens Matter* 14(11):2717–2744
48. Materials Studio Simulation Environment (2019) Release 2019. Accelrys Software Inc, San Diego, CA
49. Perdew JP, Burke K, Ernzerhof M (1996) Generalized gradient approximation made simple. *Phys Rev Lett* 77(18):3865–3868
50. Song J-W, Yamashita K, Hirao K (2011) Communication: a new hybrid exchange correlation functional for band-gap calculations using a short-range Gaussian attenuation (Gaussian–Perdew–Burke–Ernzerhof). *J Chem Phys* 135(7):071103
51. White J, Bird D (1994) Implementation of gradient-corrected exchange-correlation potentials in Car-Parrinello total-energy calculations. *Phys Rev B* 50(7):4954–4957
52. Mattila T, Nieminen RM (1996) Ab initio study of oxygen point defects in GaAs, GaN, and AlN. *Phys Rev B* 54(23):16676–16682
53. Li J, Nam K, Nakarmi M, Lin J, Jiang H, Carrier P, Wei S-H (2003) Band structure and fundamental optical transitions in wurtzite AlN. *Appl Phys Lett* 83(25):5163–5165
54. Silveira E, Freitas J, Schujman S, Schowalter L (2008) AlN band-gap temperature dependence from its optical properties. *J Cryst Growth* 310(17):4007–4010

55. Mishra V, Warshi MK, Sati A, Kumar A, Mishra V, Kumar R, Sagdeo P (2019) Investigation of temperature-dependent optical properties of TiO_2 using diffuse reflectance spectroscopy. *SN Appl Sci* 1(3):241
56. Hicks L, Dresselhaus M (1993) Effect of quantum-well structures on the thermoelectric figure of merit. *Phys Rev B* 47(19):12727–12731
57. Larson P, Mahanti S, Kanatzidis MG (2000) Electronic structure and transport of Bi_2Te_3 and BaBiTe_3 . *Phys Rev B* 61(12):8162–8171
58. Maxwell JC (1865) VIII. A dynamical theory of the electromagnetic field. *Philos Trans R Soc Lond* 155:459–512
59. Maxwell JC (1864) A dynamical theory of the electromagnetic field, vol 13. The Society, London
60. Potter R (1997) Optical properties. In: Ghosh G, Palik ED (eds) *Handbook of optical constants of solids, five-volume set: handbook of thermo-optic coefficients of optical materials with applications*. Elsevier, Amsterdam, p 11
61. Judd DB (1942) Fresnel reflection of diffusely incident light. *J Res Natl Bur Stand* 29(5):329–332
62. Clays K, Persoons A (1991) Hyper-Rayleigh scattering in solution. *Phys Rev Lett* 66(23):2980–2983
63. Williams B (1977) Compton scattering: the investigation of electron momentum distributions, vol 10. McGraw-Hill International Book Co, New York
64. Šantić B, Desnica U (1990) Thermoelectric effect spectroscopy of deep levels—application to semi-insulating GaAs. *Appl Phys Lett* 56(26):2636–2638
65. Gaur K, Lal H (1985) Electrical transport in light rare-earth vanadates. *JMatS* 20(9):3167–3176
66. Shi L, Xu C, Yuan H (2011) A CASTEP study on magnetic properties of C-doped ZnO crystal. *Phys B* 406(17):3187–3191
67. Mulliken RS (1955) Electronic population analysis on LCAO–MO molecular wave functions. I. *J Chem Phys* 23(10):1833–1840
68. Csizmadia I (1976) Theory and practice of MO calculations on organic molecules. In: Csizmadia I (ed) *Progress in theoretical organic chemistry*, vol 1. Elsevier Scientific Publishing Company, New York
69. Yuan K, Chen L, Li F, Chen Y (2014) Nanostructured hybrid $\text{ZnO}@\text{CdS}$ nanowalls grown in situ for inverted polymer solar cells. *J Mater Chem C* 2(6):1018–1027
70. Opoku F, Govender KK, van Sittert CGCE, Govender PP (2018) Insights into the photocatalytic mechanism of mediator-free direct Z-scheme $\text{g-C}_3\text{N}_4/\text{Bi}_2\text{MoO}_6(010)$ and $\text{g-C}_3\text{N}_4/\text{Bi}_2\text{WO}_6(010)$ heterostructures: a hybrid density functional theory study. *Appl Surf Sci* 427:487–498
71. Louis E, San-Fabián E, Díaz-García MA, Chiappe G, Vergés JA (2017) Are electron affinity and ionization potential intrinsic parameters to predict the electron or hole acceptor character of amorphous molecular materials? *J Phys Chem Lett* 8(11):2445–2449

Publisher's Note Springer Nature remains neutral with regard to jurisdictional claims in published maps and institutional affiliations.